48th AIAA Aerospace Sciences Meeting Including the New Horizons Forum and Aerospace Exposition
4 - 7 January 2010, Orlando, Florida

AIAA 2010-1452

Low diffusion E-CUSP scheme with high order WENO scheme for preconditioned Navier-Stokes equations

Yiqing Shen[*], Gecheng Zha[†]
Dept. of Mechanical and Aerospace Engineering
Miami Wind ^{TM}
University of Miami
Coral Gables, Florida 33124
E-mail: yqshen@miami.edu, gzha@miami.edu

Abstract

A low diffusion E-CUSP (LDE) scheme for preconditioned Navier-Stokes equations is developed. With unfactored implicit Gauss-Seidel relaxation scheme for time integration, the LDE scheme with high-order WENO reconstruction is used to simulate several flows at various speed from low speed natural convection to supersonic flows. Numerical results are presented to show efficiency, accuracy and robustness of the new preconditioning scheme.

1 Introduction

In recent years, the convective upwind and split pressure (CUSP) family schemes have achieved great success. The CUSP schemes can be basically categorized to two types, the H-CUSP and E-CUSP[1, 2, 3]. The H-CUSP schemes have the total enthalpy from the energy equation in their convective vector, while the E-CUSP schemes use the total energy in the convective vector. The Liou's AUSM family schemes[4, 5, 6, 7, 8], Van Leer-Hänel scheme[9], and Edwards's LDFSS schemes[10, 11] belong to the H-CUSP group. The schemes developed by Zha, et al.[12, 13, 14, 15, 16] belong to the E-CUSP group.

From the characteristic theory point of view, the H-CUSP schemes are not fully consistent with the disturbance propagation directions[17, 18], which may affect the stability and robustness of the schemes. By splitting the eigenvalues of the Jacobians to convection (velocity) and waves (speed of sound), one will find that the convection terms only contain the total energy[12], which will lead to the E-CUSP schemes.

With the application of computational fluid dynamics becoming more and more popular, the demand for developing a unified algorithm for compressible and incompressible flows becomes stronger to satisfy the needs of broad engineering problems. When direct applying compressible flow equation to incompressible flows, there exist two problems: stiffness and large numerical dissipation. Both problems are because of a large difference between the speed of sound and flow speed. The large dissipation may cause low convergence, distort the solution of a wall boundary layer, etc.

Preconditioning is to change the eigenvalues of the compressible flow equations system in order to remove the large disparity of wave speeds. Usually, the system of compressible flow equations is preconditioned by multiplying the time derivatives with a suitable matrix[19, 20, 21, 22, 23].

---

[*] Research Scientist, AIAA Member
[†] Associate Professor, AIAA Senior Member

For the spatial discretization with preconditioning, the 2nd order central differencing is adopted by Choi and Merkle [22, 24] and Bortoli[25]. The Roe-type flux-difference splitting (FDS) is used by Weiss and Smith [23, 26, 27, 28, 29]. The third-order MUSCL extrapolation is used by Briley et al [30]. The flux-vector splitting (FVS) is applied by Turkle et al [31]. Edwards and his colleagues [32, 33, 34, 35] have extended their H-CUSP schemes to all flow speeds. There is no work to extend E-CUSP schemes to preconditioning.

The purpose of this paper is to develop a preconditioned low diffusion E-CUSP scheme with high order WENO scheme for preconditioned Navier-Stokes equations at all flow speeds. With unfactored implicit Gauss-Seidel relaxation scheme for time integration, the LDE scheme is used to simulate various flow fields at all speeds. The numerical results of a lid driven cavity flow, a natural convective cavity flow, subsonic flow, transonic and supersonic flows show that the method of preconditioning with high-order schemes is efficient, robust, and accurate for both low speed incompressible flows and high speed compressible flows.

2 Numerical Method

2.1 Governing Equations

The preconditioned system for steady state flows in generalized coordinate is obtained by multiplying the preconditioning matrix Γ to the time derivative terms of Navier-Stokes equations to give

$$\Gamma\frac{\partial q}{\partial t}+\frac{\partial E}{\partial \xi}+\frac{\partial F}{\partial \eta}+\frac{\partial G}{\partial \zeta}=\frac{1}{Re}\left(\frac{\partial R}{\partial \xi}+\frac{\partial S}{\partial \eta}+\frac{\partial T}{\partial \zeta}\right) \tag{1}$$

The preconditioning matrix Γ has various forms[19, 21, 22, 23], and is dependent on the choice of q. This paper adopts the method of Weiss and Smith described in Ref.[23]. The q and Γ are taken as the following,

$$q=(p,u,v,w,T)^T$$

$$\Gamma=\begin{bmatrix} \Theta & 0 & 0 & 0 & \rho_T \\ \Theta u & \rho & 0 & 0 & \rho_T u \\ \Theta v & 0 & \rho & 0 & \rho_T v \\ \Theta w & 0 & 0 & \rho & \rho_T w \\ \Theta H-1 & \rho u & \rho v & \rho w & \rho_T H+\rho C_p \end{bmatrix}$$

where Θ is given by

$$\Theta=(\frac{1}{U_r^2}-\frac{\rho_T}{\rho C_p})$$

U_r is a reference velocity. In this paper, the reference velocity proposed by Edwards and Roy[32] is used:

$$U_r=min[c,max(|V|,k|V_\infty|)]$$

where, c is the speed of sound, $|V|=\sqrt{u^2+v^2+w^2}$ is the velocity magnitude, $|V_\infty|$ is a reference velocity. H is the total enthalpy, ρ_T stands for $\frac{\partial \rho}{\partial T}$, C_p is the specific heat at constant pressure. k is a constant[28].

The eigenvalues of $\Gamma^{-1}\frac{\partial E}{\partial q}$ are

$$U,U,U,U'+C',U'-C' \tag{2}$$

where

$$U=l_x u+l_y v+l_z w$$

$$U'=\frac{1}{2}U(1+M_r^2),\ C'=\frac{1}{2}\sqrt{(1-M_r^2)U^2+4M_r^2C^2}$$

and

$$M_r = \frac{U_r}{c}, \;\; C = c\sqrt{l_x^2 + l_y^2 + l_z^2}$$

l is the normal vector on ξ surfaces with its magnitude equal to the elemental surface area and pointing to the direction of increasing ξ.

$$\mathbf{l} = l_x i + l_y j + l_z k = \frac{\nabla\xi}{J} \mathrm{d}\eta \mathrm{d}\zeta \tag{3}$$

J is the transformation Jacobian. The eigenvalues given in Eq. (2) will have the same order of magnitude when the velocity approaches zero. This is the purpose of preconditioning to improve the condition number of the Jacobian and remove the stiffness.

2.2 Preconditioning of The Low Diffusion E-CUSP (LDE) Scheme

In [12, 13, 15, 16], the characteristic analysis is given as the foundation to construct the E-CUSP scheme. The basic idea is to split the flux $\mathbf{E}$ to the convective flux $\mathbf{E^c}$ and the pressure flux $\mathbf{E^p}$. That is:

$$\mathbf{E} = E^c + E^p = \begin{pmatrix} \rho U \\ \rho u U \\ \rho v U \\ \rho w U \\ \rho e U \end{pmatrix} + \begin{pmatrix} 0 \\ l_x p \\ l_y p \\ l_z p \\ p U \end{pmatrix} \tag{4}$$

The convective flux, $E^{1/2}$ is evaluated as,

$$E_{1/2} = E^c_{1/2} + E^p_{1/2} \tag{5}$$

where

$$E^c_{1/2} = U^+ f^c_L + U^- f^c_R \tag{6}$$

and

$$E^p_{\frac{1}{2}} = p_{1/2} \begin{pmatrix} 0 \\ l_x \\ l_y \\ l_z \\ U_{1/2} \end{pmatrix}, \qquad f^c = \begin{pmatrix} \rho \\ \rho u \\ \rho v \\ \rho w \\ \rho e \end{pmatrix} \tag{7}$$

$$p_{1/2} = P^+ p_L + P^- p_R \tag{8}$$

The different formulations for U^+, U^-, P^+ and P^- can be found in[12, 13, 15, 16] by different requirements.

The preconditioning of the the LDE scheme needs to satisfy two conditions when the flow velocity approaching zero: 1) the eigenvalues of the Jacobian matrices are at the same order of magnitude of the velocity, 2) numerical dissipation will diminish. The condition 1 is explained in the previous section. The condition 2 is analyzed as the following.

The interface flux $F_{1/2}$ can be generally defined as consisting of a central difference contribution plus a diffusive contribution $\mathbf{D}$ as[32]

$$F_{1/2} = \frac{1}{2}\left[F_L + F_R + \mathbf{D}(L, R)\right] \tag{9}$$

Similarly, the interface pressure $p_{1/2}$ of (8) can be written as[34]

$$p_{1/2} = P^+ p_L + P^- p_R = \frac{1}{2}\left[(p_L + p_R) + (P^+ - P^-)(p_L - p_R) + (P^+ + P^- - 1)(p_L + p_R)\right] \tag{10}$$

The last two term can be regarded as the diffusion terms of $p_{1/2}$. Low Mach number results in large pressure value, hence the second difussion term may be excessively large. A better scaling is found by replacing $(p_L + p_R)$ by $2\rho_{1/2}\tilde{c}^2_{1/2}$ or $2\rho_{1/2}U^2_{r,1/2}$[33, 34]. That is, Eq. (10) is replaced by

$$p_{1/2} = P^+ p_L + P^- p_R = \frac{1}{2}\left[(p_L + p_R) + (P^+ - P^-)(p_L - p_R) + \rho_{1/2}U^2_{r,1/2}(P^+ + P^- - 1)\right] \tag{11}$$

Similarly, the split velocities $U^\pm$ used in the low-diffusion flux splitting scheme can be written as

$$U^+ = \tilde{c}_{1/2}[M^+ - M^+_{1/2}]$$

$$U^- = \tilde{c}_{1/2}[M^- + M^-_{1/2}]$$

where

$$M^+_{1/2} = M_{1/2}\left(1 - \frac{p_L - p_R + \delta|p_L - p_R|}{p_L + p_R}\right) \tag{12}$$

$$M^-_{1/2} = M_{1/2}\left(1 + \frac{p_L - p_R - \delta|p_L - p_R|}{p_L + p_R}\right) \tag{13}$$

Using $2\rho_L U^2_{r,1/2}$ and $2\rho_R U^2_{r,1/2}$ to replace $(p_L + p_R)$ in Eqs. (12) and (13), respectively, the new split velocities are obtained as

$$U^+ = \tilde{c}_{1/2}\left[M^+ - M_{1/2}(1 - \frac{p_L - p_R + \delta|p_L - p_R|}{2\rho_L U^2_{r,1/2}})\right] \tag{14}$$

$$U^- = \tilde{c}_{1/2}\left[M^- + M_{1/2}(1 + \frac{p_L - p_R - \delta|p_L - p_R|}{2\rho_R U^2_{r,1/2}})\right] \tag{15}$$

$\delta = 1$ is used in [34], $\delta = 0$ is used in [35] and also in this paper.

Other quantities used in the preceding definitions are

$$M^+ = \alpha^+_L(1 + \beta_L)M_L + \beta_L M^+_L$$

$$M^- = \alpha^-_R(1 + \beta_R)M_R - \beta_R M^-_R$$

$$M^\pm_{L,R} = \pm\frac{1}{4}(M_{L,R} \pm 1)^2$$

$$\alpha^\pm_{L,R} = \frac{1}{2}[1 \pm sign(1.0, M_{L,R})]$$

$$\beta_{L,R} = -max[0, 1 - int(|M_{L,R}|)]$$

$$M_{1/2} = \frac{1}{2}(M^+ - \alpha^+_L M_L - M^- + \alpha^-_R M_R)$$

$$P^\pm = \alpha^\pm_{L,R}(1 + \beta_{L,R}) - \frac{\beta_{L,R}}{2}[1 \pm M_{L,R}]$$

$$\tilde{c}_{1/2} = \frac{\sqrt{(1 - M_r^2)^2U^2 + 4C^2M_r^2}}{1 + M_r^2}|_{1/2}$$

and

$$M_{L,R} = \frac{U_{L,R}}{\tilde{c}_{1/2}}$$

As stated in section 1, the difference between the H-CUSP scheme and E-CUSP scheme is that, the H-CUSP scheme uses the total enthalpy and the E-CUSP scheme uses the total energy in Eq.(4) for the convective vector. Hence, H-CUSP schemes[32, 34, 35] do not have the term of $p_{1/2}U_{1/2}$ in Eq. (7). In this paper, the interface velocity $U_{1/2}$ is evaluated as

$$U_{1/2} = U^+ + U^- \tag{16}$$

2.3 The WENO reconstruction

The high order accuracy of $E_{i+1/2}$ is obtained by achieving the high order accuracy of the left and right primitive variables q^L and q^R using the WENO scheme described below. This procedure is similar to the MUSCL scheme suggested by van Leer[36] and is adopted in [37].

The finite difference 5th-order accuracy WENO scheme suggested by Jiang and Shu [38] is used to evaluate the primitive variables q^L and q^R. The WENO scheme for variable q^L can be written as:

$$q^L_{i+1/2} = \omega_0 q_0 + \omega_1 q_1 + \omega_2 q_2 \tag{17}$$

where ω_0, ω_1 and ω_2 are the weights, and the q_0, q_1 and q_2 are the 3rd order accuracy reconstruction of the variables in three different stencils. They are determined as the following,

$$q_0 = \frac{1}{3}q_{i-2} - \frac{7}{6}q_{i-1} + \frac{11}{6}q_i$$

$$q_1 = -\frac{1}{6}q_{i-1} + \frac{5}{6}q_i + \frac{1}{3}q_{i+1}$$

$$q_2 = \frac{1}{3}q_i + \frac{5}{6}q_{i+1} - \frac{1}{6}q_{i+2}$$

and

$$\omega_k = \frac{\alpha_k}{\alpha_0 + \cdots + \alpha_{r-1}}, \tag{18}$$

$$\alpha_k = \frac{C_k}{(\varepsilon + IS_k)^p}, \quad k = 0, 1, 2 \tag{19}$$

where C_k are the optimal weights with the following values:

$$C_0 = 0.1, \quad C_1 = 0.6, \quad C_2 = 0.3$$

The IS_k are the smooth estimators determined as

$$\begin{array}{l} IS_0 = \frac{13}{12}(q_{i-2} - 2q_{i-1} + q_i)^2 + \frac{1}{4}(q_{i-2} - 4q_{i-1} + 3q_i)^2 \\ IS_1 = \frac{13}{12}(q_{i-1} - 2q_i + q_{i+1})^2 + \frac{1}{4}(q_{i-1} - q_{i+1})^2 \\ IS_2 = \frac{13}{12}(q_i - 2q_{i+1} + q_{i+2})^2 + \frac{1}{4}(3q_i - 4q_{i+1} + q_{i+2})^2 \end{array} \tag{20}$$

The ε in Eq.(19) is introduced to avoid the denominator becoming zero. Jiang and Shu's numerical tests indicate that the results are not sensitive to the choice of ε as long as it is in the range of 10^{-5} to 10^{-7}. In their paper[38], ε is taken as 10^{-6}. In Ref. [37], the ε value of 10^{-2} suggested by Shen et al to suppress the oscillation of IS_k and improve the convergence and accuracy is adopted in this paper.

The q^R is constructed symmetrically as q^L about $i + 1/2$.

2.4 The 4th-Order Schemes for Viscous Terms[39]

A set of fully conservative 4th-order accurate finite central differencing schemes using the same stencil width of the WENO scheme for the viscous terms is used in this paper. The scheme for the viscous derivative term $\frac{\partial R}{\partial \xi}$ in Navier-Stokes equations Eq.(1) can be written as the following,

$$\frac{\partial R}{\partial \xi}|_i = \frac{\tilde{R}_{i+1/2} - \tilde{R}_{i-1/2}}{\Delta \xi} \tag{21}$$

To obtain 4th order accuracy, $\tilde{R}$ needs to be reconstructed as

$$\tilde{R}_{i-1/2} = \sum_{I=i-3/2}^{i+1/2} \alpha_I R_I \tag{22}$$

where

$$\begin{aligned}
&\alpha_{i-3/2} = -\frac{1}{24},\ \alpha_{i-1/2} = \frac{26}{24},\ \alpha_{i+3/2} = -\frac{1}{24} \\
&R_{i-1/2} = [(\xi_x \tau_{xx}) + (\eta_y \tau_{xy}) + (\zeta_z \tau_{xz})]_{i-1/2} \\
&\begin{aligned}(\tau_{xx}) = \quad & \mu\{\tfrac{4}{3}\left[(\xi_x \tfrac{\partial u}{\partial \xi}) + (\eta_x \tfrac{\partial u}{\partial \eta}) + (\zeta_x \tfrac{\partial u}{\partial \zeta})\right] \\
& -\tfrac{2}{3}[(\xi_y \tfrac{\partial v}{\partial \xi}) + (\eta_y \tfrac{\partial v}{\partial \eta}) + (\zeta_y \tfrac{\partial v}{\partial \zeta}) \\
& (\xi_z \tfrac{\partial w}{\partial \xi}) + (\eta_z \tfrac{\partial w}{\partial \eta}) + (\zeta_z \tfrac{\partial w}{\partial \zeta})]\}\end{aligned}
\end{aligned} \tag{23}$$

If R_I in Eq.(22) can be approximated with the accuracy order not lower than 4th order, the Taylor expansion analysis of (21) and (22) will give the following relation[39],

$$\frac{1}{\Delta\xi}(\tilde{R}_{i+1/2} - \tilde{R}_{i-1/2}) = R^{'}(\xi_i) + O(\Delta\xi^4) \tag{24}$$

i.e. the 4th order accuracy is achieved.

In order to achieve the highest order accuracy of R_I with $I = i-3/2, i-1/2, i+1/2$, the approximation of each component in Eq. (22) using all the involved points of the WENO stencil is given below:

$$\mu_I = \sum_{l=m}^{n} C_l^I \mu_{i+l}, \tag{25}$$

$$\frac{\partial u}{\partial \xi}|_I = \frac{1}{\Delta\xi} \sum_{l=r}^{s} D_l^I u_{i+l}, \tag{26}$$

$$\frac{\partial u}{\partial \eta}|_I = \sum_{l=m}^{n} C_l^I \frac{\partial u}{\partial \eta}|_{i+l,j} \tag{27}$$

where

$$\frac{\partial u}{\partial \eta}|_{i,j} = \frac{1}{\Delta\eta} \sum_{l=p}^{q} C_l^c u_{i,j+l}, \tag{28}$$

By choosing different ranges for $(m,n), (r,s), (p,q)$ and different coefficients C_l^I, D_l^I, C_l^c, one can obtain different order accuracy approximation to the viscous terms. The principle of choosing $(m,n), (r,s), (p,q)$ is to ensure that the approximation of $\frac{\partial R}{\partial \xi}|_i$ in Eq.(21) is a central differencing. For example, in this paper, $(m,n) = (-2,1), (r,s) = (-3,2), and\ (p,q) = (-2,2)$ are used, and they give[39],

$$\mu_I = \sum_{l=m}^{n} C_l^I \mu_{i+l} + O(\Delta\xi^4), \tag{29}$$

$$\frac{\partial u}{\partial \xi}|_I = \frac{1}{\Delta\xi} \sum_{l=r}^{s} D_l^I u_{i+l} + O(\Delta\xi^5), \tag{30}$$

$$\frac{\partial u}{\partial \eta}|_I = \sum_{l=m}^{n} C_l^I \frac{\partial u}{\partial \eta}|_{i+l,j} + O(\Delta\xi^4, \Delta\eta^4), \tag{31}$$

where

$$\frac{\partial u}{\partial \eta}|_{i,j} = \frac{1}{\Delta\eta} \sum_{l=p}^{q} C_l^c u_{i,j+l} + O(\Delta\eta^4) \tag{32}$$

the coefficients C_l^I, D_l^I, C_l^c can be obtained by Taylor's series expansion and are given in Tables 1-3.

Table 1: The coefficients of C_l^I

I	C_{-2}^I	C_{-1}^I	C_0^I	C_1^I
$i-3/2$	5/16	15/16	-5/16	1/16
$i-1/2$	-1/16	9/16	9/16	-1/16
$i+1/2$	1/16	-5/16	15/16	5/16

Table 2: The coefficients of D_l^I

I	D_{-3}^I	D_{-2}^I	D_{-1}^I	D_0^I	D_1^I	D_2^I
$i-3/2$	71/1920	-141/128	69/64	1/192	-3/128	3/640
$i-1/2$	-3/640	25/384	-75/64	75/64	-25/384	3/640
$i+1/2$	-3/640	3/128	-1/192	-69/64	141/128	-71/1920

3 Time Marching Method

The implicit discretized formula of Eq.(1) can be expressed as following,

$$\left(\frac{\Gamma}{\Delta t} + \frac{\partial RHS}{\partial q}|'\right)\delta q^{n+1} = RHS^n \tag{33}$$

where RHS is the redidual calculated by using inviscid numerical fluxes and viscous fluxes, such as Eqs. (5)and (21), $\frac{\partial RHS}{\partial q}|'$ is the approximation of Jacobian matrix $\frac{\partial RHS}{\partial q}$.

A first order discretization is used for solving the corresponding Jacobian matrices on the left hand side of Eq. (33). For example, for convective flux $E_{i+1/2}$,

$$\frac{\partial E_{i+1/2}}{\partial q_{i+1/2}}\delta q_{i+1/2} = \frac{1}{2}\left[\frac{\partial E}{\partial q}|_i + \left(\Gamma M_\Gamma|\Lambda_\Gamma|M_\Gamma^{-1}\right)|_{i+1/2}\right]\delta q_i + \frac{1}{2}\left[\frac{\partial E}{\partial q}|_{i+1} - \left(\Gamma M_\Gamma|\Lambda_\Gamma|M_\Gamma^{-1}\right)|_{i+1/2}\right]\delta q_{i+1} \tag{34}$$

where, Λ_Γ is the diagonal matrix of eigenvalues Eq. (2), M_Γ and M_Γ^{-1} are the matrices of right and left eigenvectors[29]. The second order central differencing is used for viscous flux $R_{i+1/2}$ on the left hand side of Eq. (33), and the Jacobian matrix is follows,

$$\frac{\partial R_{i+1/2}}{\partial q_{i+1/2}}\delta q_{i+1/2} = \frac{\partial R_{i+1/2}}{\partial q_i}\delta q_i + \frac{\partial R_{i+1/2}}{\partial q_{i+1}}\delta q_{i+1} \tag{35}$$

The final linearized equations of Eq. (33) can be written as the following,

$$\begin{gathered}\bar{B}\Delta q_{i,j,k}^{n+1} + A^+\Delta q_{i+1,j,k}^{n+1} + A^-\Delta q_{i-1,j,k}^{n+1} + B^+\Delta q_{i,j+1,k}^{n+1} + B^-\Delta q_{i,j-1,k}^{n+1} + \\ C^+\Delta q_{i,j,k+1}^{n+1} + C^-\Delta q_{i,j,k-1}^{n+1} = RHS^n\end{gathered} \tag{36}$$

where

$$\bar{B} = \Gamma + A + B + C$$

and

$$A = \frac{\Delta t}{J}[(\hat{A}_{i+1/2}^L - L_{i+1/2}^L) - (\hat{A}_{i-1/2}^R - L_{i-1/2}^R)]$$

$$A^+ = \frac{\Delta t}{J}(\hat{A}_{i+1/2}^R - L_{i+1/2}^R), \qquad A^- = -\frac{\Delta t}{J}(\hat{A}_{i-1/2}^L - L_{i-1/2}^L)$$

Table 3: The coefficients of C_l^c

C_{-2}^c	C_{-1}^c	C_0^c	C_1^c	C_2^c
1/12	-8/12	0	8/12	-1/12

$$\hat{A}_{i+1/2}^R = \frac{1}{2}(A_{i+1} - \tilde{A}_{i+1/2}), \qquad \hat{A}_{i+1/2}^L = \frac{1}{2}(A_i + \tilde{A}_{i+/2})$$

$$A_i = \frac{\partial E}{\partial q}|_i, \qquad \tilde{A}_{i+1/2} = \left(\Gamma M_\Gamma |\Lambda_\Gamma| M_\Gamma^{-1}\right)|_{i+1/2}$$

$$L_{i+1/2}^L = \frac{\partial R_{i+1/2}}{\partial q_i}, \qquad L_{i+1/2}^R = \frac{\partial R_{i+1/2}}{\partial q_{i+1}}$$

J is the transformation Jacobian. $B^\pm$, B and $C^\pm$, C have the same forms as $A^\pm$, A. And,

$$\begin{aligned} RHS^n = \; & \tfrac{\Delta t}{J}[(R_{i+1/2}^n - R_{i-1/2}^n) + (S_{j+1/2}^n - S_{j-1/2}^n) + (T_{k+1/2}^n - T_{k-1/2}^n) \\ & -(E_{i+1/2}^n - E_{i-1/2}^n) - (F_{j+1/2}^n - F_{j-1/2}^n) - (G_{k+1/2}^n - G_{k-1/2}^n)] \end{aligned} \tag{37}$$

The Gauss-Seidel line iteration in a certain sweep direction, for example, in ξ direction assuming the sweeping from small index value to large one, can be written as

$$B^- \Delta q_{i,j-1,k}^{n+1} + \bar{B} \Delta q_{i,j,k}^{n+1} + B^+ \Delta q_{i,j+1,k}^{n+1} = RHS' \tag{38}$$

where,

$$RHS' = RHS^n - A^+ \Delta q_{i+1,j,k}^n - A^- \Delta q_{i-1,j,k}^{n+1} - C^+ \Delta q_{i,j,k+1}^n - C^- \Delta q_{i,j,k-1}^{n+1} \tag{39}$$

4 Results and Discussion

To demonstrate the effectiveness of the preconditioned LDE scheme, the test cases include a lid driven cavity, a cavity natural convection flow, a subsonic flat plate turbulent boundary layer, inviscid transonic converging-diverging nozzle flow, the transonic flow over RAE2822 airfoil, and the laminar wall boundary layer with Mach number from 10^{-3} to 2.0.

In this paper, at boundaries, the conservative variables are first obtained using various required boundary conditions[37], and then the primitive variables used in preconditioning system are calculated from the conservation variables accordingly.

In this paper, the residual is defined as

$$Residual = Max\{|RHS^n|\}_{ijk}$$

and RHS^n is determined by Eq.(37).

4.1 Lid Driven Cavity Flow

The lid driven cavity flow is a benchmark solution used to validate incompressible flow calculation[28, 40, 41]

The flowfiled with Reynolds of 3200, no-slip isothermal wall boundary condition and a Mach number of 10^{-3} for the moving lid is calculated. For the purpose of comparison, the uniform mesh systems of 100 × 100, 200 × 200.

Fig. 1 gives the convergence histories. Since the primitive pressure p is used in the present preconditioned method, the decreasing Mach number results in the increased machine round errors, which increases proportionally with M^2[29, 22]. From Fig. 1, it can be seen that the residual is still decreased about $8 \sim 9$ order of magnitude. It is worthy pointing out that the method without preconditioning can not get the correct solution for this case due to excessive dissipation.

Fig. 2 is the comparison of u velocity along the vertical centerline. The present results are in good agreement with that obtained by incompressible eqution[40].

Fig. 3 shows the streamlines calculated by the present method with the mesh of 100×100. It exhibits a large primary vortex with two secondary vortices in the two bottom corners and a secondary vortex near the upper-left corner, which is the same as other researchers predict[28, 40, 41].

4.2 Cavity Natural Convection Flow

The second test case is a cavity natural convection flow induced by a temperature difference of 4 times on the two vertical walls. This flow has very low velocity and is completely in the incompressible flow regime. The configuration consists of two insulated horizontal walls and two vertical walls at temperature T_h and T_c, $T_h = 4T_c$. In this paper, the natural convective flows at two Rayleigh number, $Ra = 10^3$ and $Ra = 10^5$, are calculated. The uniform mesh with size of 100×100 is used.

The convergence histories are shown in Fig. 4. Fig. 5 compares the Nusselt number at the left side wall with the result of Chenoweth-Paolucci[42] and Choi-Merkle[22], they are in excellent agreement. Figs. 6-9 show the streamline and temperature isolines. Fig. 7 and 9 indicate that the flow evolves from one vortex core to two vortex cores when the Rayleigh number is increased from 10^3 to 10^5. This is due to the instability induced by high Rayleigh number, and is consistent with the solutions obtained by other researchers[22].

Same as the first test case, without preconditioning, it can not obtained the correct solution.

4.3 Wall Boundary Layer

The third validation case is a steady state laminar boundary layer flow on an adiabatic flat plate to test the methodology for both compressible and incompressible flows. The Reynolds number based on the length of the flat plate is 4.0×10^4. The Prandtl number of 1.0 is used in order to compare with the analytical solution. The computation domain is taken to be $[0, 2] \times [0, 1.6]$. The mesh size is 180×80.

Three cases with different incoming Mach number ($M_\infty = 2.0$, $M_\infty = 10^{-2}$, and $M_\infty = 10^{-3}$) are calculated:

Fig. 10 is the convergence histories of the case with Mach number of 2.0, the supersonic flat plate laminar flow, with and without preconditioning. It shows that the precondition method has the same convergence rate as the one without preconditioning. For this supersonic flow, the thin subsonic boundary layer has created little stiffness and hence the advantage of preconditioning is not significant.

The computed velocity and temperature profiles of this supersonic laminar boundary layer shown in Figs. 11 and 12 indicate that the numerical results agree excellently with the Blasius solution.

Figs. 13 and 14 show the convergence histories of the cases with $M = 10^{-2}$ and $M = 10^{-3}$. It can be seen that the residual without preconditioning oscillate with a large amplitude. For the cases with $M_\infty = 10^{-2}$, the residual with preconditioning is about 6 orders of magnitude lower than the one without preconditioning. For the case with $M_\infty = 10^{-3}$, the residual with preconditioning keeps reducing within a small oscillation.

Figs. 15 and 16 are the comparison of numerical results with Blasius solution for $M = 10^{-2}$ and

10^{-3}. Figs. 15 shows that, though its solution is less accurate than the preconditioned one, the flow solver without preconditioning can still resolve the boundary layer at $M = 10^{-2}$. However, the velocity profile in Fig. 16 demonstrates that, for the case with $M = 10^{-3}$, the numerical solution without preconditioning is significantly diffused due to the large numerical dissipation, whereas the preconditioned solvers accurately resolve the velocity profile.

4.4 Transonic Converging-Diverging Nozzle

To examine the performance of the preconditioning methodology in two-dimensional flow and the capability to capture shock waves, an inviscid transonic converging-diverging nozzle is calculated. The nozzle was designed and tested at NASA and was named as Nozzle A1[43]. Due to the geometric symmetry about the center line, only the upper half of the nozzle is calculated. The mesh size is 175×50. The grid is clustered near the wall. The inlet Mach number is 0.28.

Fig. 19 shows the Mach contours obtained by present preconditioning method. Fig. 17 is the comparison of the convergence histories with and without precondition. Similar to the flow of subsonic flat plate turbulent boundary layer, the preconditioned convergence rate is again about 20% faster than the one without preconditioning.

Fig. 18 shows the pressure coefficients at the upper wall surface. It can be seen that both the methods with and without preconditioning obtain identical results.

4.5 Transonic RAE2822 Airfoil

To further examine the preconditioning method for transonic compressible flows, the steady state solution of the transonic RAE2822 airfoil is calculated using the Reynolds averaged Navier-Stokes equations with the Baldwin-Lomax turbulence model. The mesh size is 256×55, the freestream Mach number M_∞ is 0.729, the Reynolds number based on chord is 6.5×10^6, and the angle of attack is 2.31^o.

From Fig. 20, we can see that the preconditioning method only needs about half of the iteration numbers of the one without preconditioning to converge to machine zero.

Figs. 21 is the comparisons of the coefficients of pressure on the wall. They show that both the results with and without preconditioning are identical and are in excellent agreement with the experiment.

Fig. 22 shows the pressure contours obtained by the present preconditioning method.

5 Conclusions

A low diffusion E-CUSP (LDE) scheme is developed for preconditioned Navier-Stokes equations. Different from H-CUSP schemes, the pressure term is separated from the total enthalpy in the energy equation and is also preconditioned in the E-CUSP scheme. Combined with the 5th-order WENO scheme for inviscid flux and the unfactored implicit Gauss-Seidel relaxation scheme for time integration, the algorithm is used to calculate flow fields from very low speed incompressible flows to supersonic compressible flows.

The numerical simulation of lid-driven and natural convective incompressible cavity flows, low subsonic incompressible flows, transonic and supersonic compressible flows show that the preconditioning method is efficient, accurate and robust, not only for the low Mach number incompressible flows, but also for the subsonic and transonic compressible flows. For high subsonic and transonic flows, the preconditioning also accelerates convergence due to reduced stiffness in near wall low speed region. For low speed incompressible flows, the preconditioning is necessary not only to remove the stiffness, but also to reduce numerical dissipation to ensure accurate results.

6 Acknowledgment

This work is supported by Miami Wind ^{TM} Research Center at University of Miami.

References

[1] A. Jameson, "Analysis and Design of Numerical Schemes for Gas Dynamics I: Artificial Diffusion, Upwind Biasing, Limiters and Their Effect on Accuracy and Multigrid Convergence in Transonic and Hypersonic Flow." AIAA Paper 93-3359, July, 1993.

[2] A. Jameson, "Analysis and Design of Numerical Schemes for Gas Dynamics I: Artificial Diffusion, Upwind Biasing, Limiters and Their Effect on Accuracy and Multigrid Convergence in Transonic and Hypersonic Flow," *Journal of Computational Fluid Dynamics*, vol. 4, pp. 171–218, 1995.

[3] A. Jameson, "Analysis and Design of Numerical Schemes for Gas Dynamics II: Artificial Diffusion and Discrete Shock Structure," *Journal of Computational Fluid Dynamics*, vol. 5, pp. 1–38, 1995.

[4] M.-S. Liou and C. J. Steffen, "A New Flux Splitting Scheme," *Journal of Computational Physics*, vol. 107, pp. 1–23, 1993.

[5] Y. Wada and M.-S. Liou, "An Accurate and Robust Splitting Scheme for Shock and Contact Discontinuities." AIAA Paper 94-0083, 1994.

[6] M.-S. Liou, "Progress Towards an Improved CFD Methods: AUSM$^+$." AIAA Paper 95-1701-CP, June, 1995.

[7] M.-S. Liou, "A Sequel to AUSM: AUSM$^+$," *Journal of Computational Physics*, vol. 129, pp. 364–382, 1996.

[8] M.-S. Liou, "Ten Years in the Making-AUSM-Family." AIAA 2001-2521, 2001.

[9] D. Hänel, R. Schwane, and G. Seider, "On the Accuracy of Upwind Schemes for the Solution of the Navier-Stokes Eqautions." AIAA paper 87-1105 CP, 1987.

[10] J. R. Edwards, "A Low-Diffusion Flux-Splitting Scheme for Navier-Stokes Calculations." AIAA Paper 95-1703-CP, June, 1995.

[11] J. R. Edwards, "A Low-Diffusion Flux-Splitting Scheme for Navier-Stokes Calculations," *Computer & Fluids*, vol. 6, pp. 635–659, 1997.

[12] G.-C. Zha and E. Bilgen, "Numerical Solutions of Euler Equations by Using a New Flux Vector Splitting Scheme ," *International Journal for Numerical Methods in Fluids*, vol. 17, pp. 115–144, 1993.

[13] G.-C. Zha, "Numerical Tests of Upwind Scheme Performance for Entropy Condition ," *AIAA Journal*, vol. 37, pp. 1005–1007, 1999.

[14] G.-C. Zha, "Comparative Study of Upwind Scheme Performance for Entropy Condition and Discontinuities." AIAA Paper 99-CP-3348, June 28- July 1, 1999.

[15] G.-C. Zha and Z.-J. Hu, "Calculation of Transonic Internal Flows Using an Efficient High Resolution Upwind Scheme," *AIAA Journal*, vol. 42, No. 2, pp. 205–214, 2004.

[16] G. -C. Zha, Y. Q. Shen, B. Y. Wang, "Calculation of Transonic Flows Using WENO Method with a Low Diffusion E-CUSP Upwind Scheme." AIAA Paper 2008-0745, Jan 2008.

[17] G.-C. Zha, "A Low Diffusion Efficient Upwind Scheme ," *AIAA Journal*, vol. 43, pp. 1137–1140, 2005.

[18] G.-C. Zha, "A Low Diffusion E-CUSP Upwind Scheme for Transonic Flows." AIAA Paper 2004-2707, to appear in AIAA Journal, 34th AIAA Fluid Dynamics Conference, June 28 - July 1 2004.

[19] E. Turkel, "Preconditioned methods for solving the incompressible and low speed compressible equations," *Journal of Computational Physics*, vol. 72, pp. 277–298, 1987.

[20] C.L. Merkle, Y.H. Choi, "Computation of low-speed compressible flows with time-marching procedures," *International Journal for Numerical Methods in Engineering*, vol. 25, pp. 293–311, 1988.

[21] E. Turkel, "Preconditioning techniques in computational fluid dynamics," *Annu. Rev. Fluid Mech.*, vol. 31, pp. 385–416, 1999.

[22] Y. H. Choi and C. L. Merkle, "The Application of Preconditioning in Viscous Flows," *Journal of Computational Physics*, vol. 105, pp. 207–223, 1993.

[23] J.M. Weiss, and W.A. Smith, "Preconditioning Applied to Variable and Constant Density Flows," *AIAA Journal*, vol. 33, pp. 2050–2057, 1995.

[24] C.L. Merkle, J.Y. Sullivan, P.E.O. Buelow and S. Venkateswaran, "Computation of Flows with Arbitrary Equations of State," *AIAA Journal*, vol. 36, pp. 515–521, 1998.

[25] A. L. De Bortoli, "Multigrid based aerodynamical simulations for the NACA 0012 airfoil," *Applied Numerical Mathematics*, vol. 40, pp. 337–349, 2002.

[26] J.M. Weiss, J.P. Maruszewski, W.A. Smith, "Implicit solution of preconditioned Navier-Stokes equations using algebraic multigrid," *AIAA Journal*, vol. 37, pp. 29–36, 1999.

[27] C. -C. Rossow, "Efficient computation of compressible and incompressible flows," *Journal of Computational Physics*, vol. 220, pp. 879–899, 2007.

[28] J.-C. Huang, H. Lin, and J.-Y. Yang, "Implicit preconditioned WENO scheme for steady viscous flow computation," *Journal of Computational Physics*, vol. 228, pp. 420–438, 2009.

[29] Y. Q. Shen, G. -C. Zha, "Simulation of Flows at All Speeds with High-Order WENO Schemes and Preconditioning." 47th AIAA Aerospace Sciences Meeting, AIAA-2009-1312, Jan 2009.

[30] W. R. Briley, L. K. Taylor, D. L. Whitfield, "High-resolution viscous flow simulations at arbitrary Mach number," *Journal of Computational Physics*, vol. 184, pp. 79–105, 2003.

[31] E. Turkel, R. Radespiel, N. Kroll, "Assessment of preconditioning methods for multidimensional aerodynamics," *Computers & Fluids*, vol. 26, pp. 613–634, 1997.

[32] J.R. Edwards,M.-S. Liou, "Low-Diffusion Flux-Splitting Methods for Flows at All Speeds," *AIAA Journal*, vol. 36, pp. 1610–1617, 1998.

[33] J. Edwards, R. Franklin, and M.-S. Liou, "Low Diffusion Flux-Splitting Methods for Real Fluid Flows with Phase Transitions," *AIAA Journal*, vol. 38, pp. 1624–1633, 2000.

[34] Mao, D., and Edwards, J. R., and Kuznetsov, A. V., and Srivastava, R. K. , "Development of low-diffusion flux-splitting methods for dense gas-solid flows," *Journal of Computational Physics*, vol. 185, pp. 100–119, 2003.

[35] Neaves, M. D., and Edwards, J. R., "All-speed time-accurate underwater projectile calculations using a preconditioning algorithm," *Journal of fluids engineering*, vol. 128, pp. 284–296, 2006.

[36] B. Van Leer, “Towards the Ultimate Conservative Difference Scheme, III,” *Journal of Computational Physics*, vol. 23, pp. 263–75, 1977.

[37] Y.-Q. Shen, G.-C. Zha, and B.-Y. Wang, “Improvement of Stability and Accuracy of Implicit WENO Scheme,” *AIAA Journal*, vol. 47, pp. 331–344, 2009.

[38] G.S. Jiang, and C.W. Shu, “Efficient implementation of weighted ENO schemes,” *J.Comput.Phys.*, vol. 126, pp. 202–228, 1996.

[39] Y. Q. Shen, G. Z. Zha, X. Y. Chen , “High order conservative differencing for viscous terms and the application to vortex-induced vibration flows,” *Journal of Computational Physics*, vol. 228, pp. 8283–8300, 2009.

[40] U. Ghia and K. N. Ghia and C. T. Shin, “High-Re solutions for incompressible flow using the Navier-Stokes equations and a multigrid method,” *Journal of Computational Physics*, vol. 48, pp. 387–411, 1982.

[41] Sheng-Tao Yu and Bo-Nan Jiang and Nan-Suey Liu and Jie Wu , “The least-squares finite element method for low-mach-number compressible viscous flows,” *International Journal for Numerical Methods in Engineering*, vol. 38, pp. 3591–3610, 1995.

[42] D. R. Chenoweth and S. Paolucci, “Natural convection in an enclosed vertical air layer with large horizontal temperature differences,” *J. Fluid Mech.*, vol. 169, pp. 173–210, 1986.

[43] Mason, M. L. and Putnam, L. E. , “The Effect of Throat Contouring on Two-Dimensional Converging-Diverging Nozzles at Static Conditions .” NASA Technical Paper 1704, 1980.

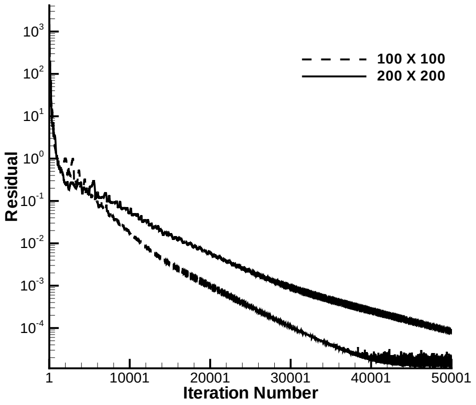

Figure 1: Convergence rate of the lid-driven cavity flow, $Re = 3200,\ M = 10^{-3}$.

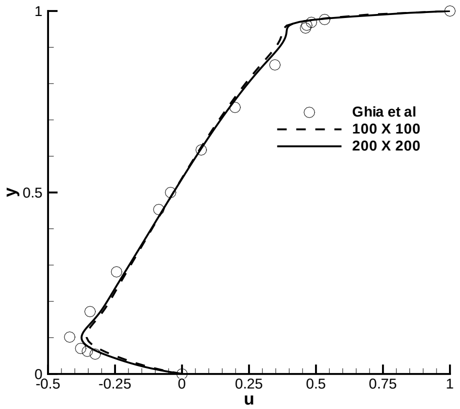

Figure 2: Velocity u along the vertical centerline for the lid driven cavity flow, $Re = 3200,\ M = 10^{-3}$.

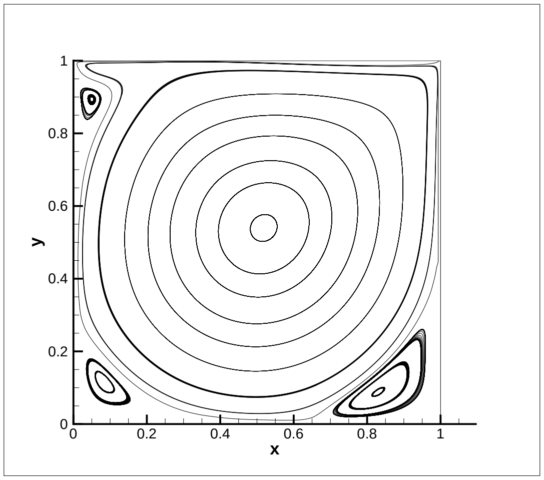

Figure 3: Streamlines for the lid driven cavity flow, 100×100.

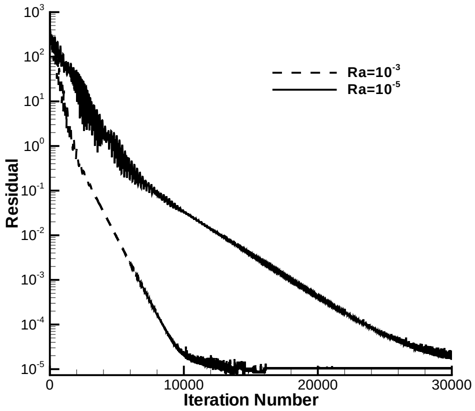

Figure 4: Convergence rate of the cavity natural convection flows

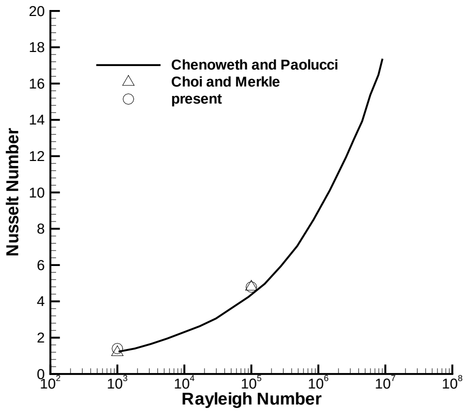

Figure 5: Comparison of Nusselt number of the cavity natural convection flow

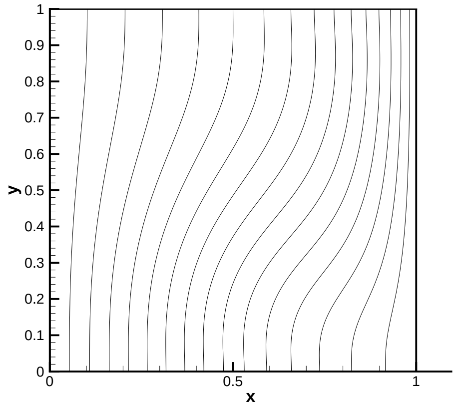

Figure 6: Isoline temperature of the cavity natural convection flow, $Ra = 10^3$

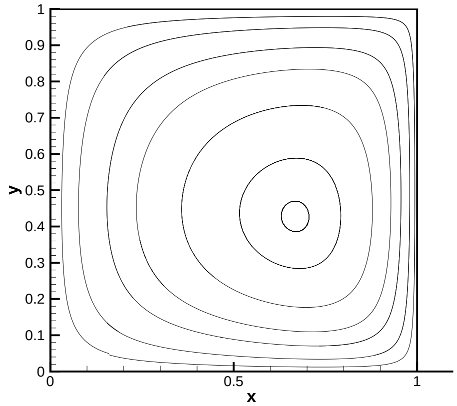

Figure 7: Streamline of the cavity natural convection flow, $Ra = 10^3$

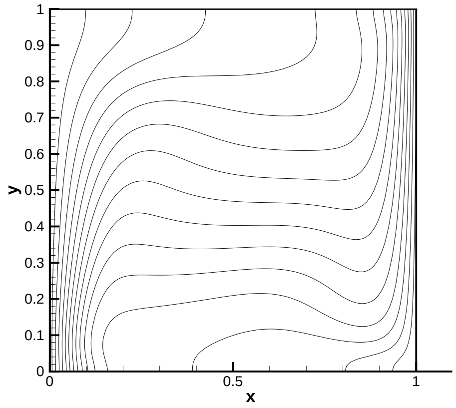

Figure 8: Isoline temperature of the cavity natural convection flow, $Ra = 10^5$

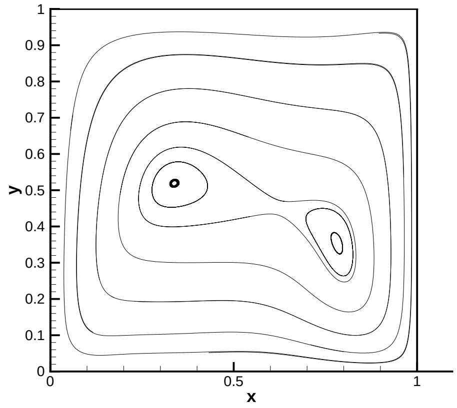

Figure 9: Streamline of the cavity natural convection flow, $Ra = 10^5$

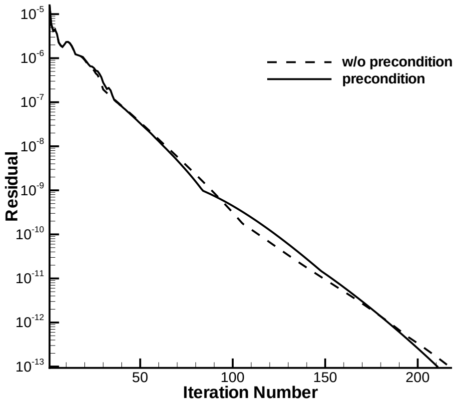

Figure 10: Convergence rate of the supersonic boundary layer flow, $M = 2.0$

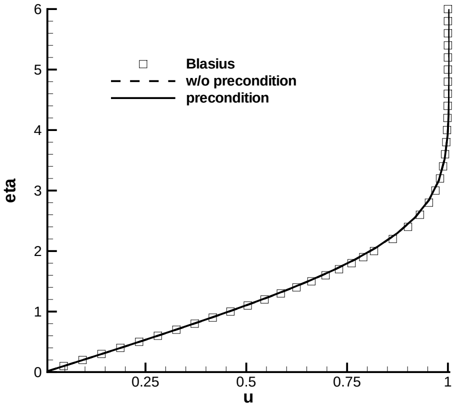

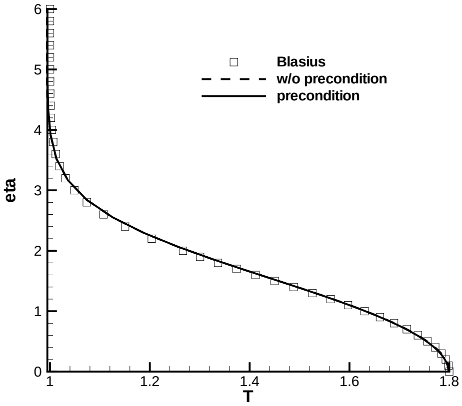

Figure 11: Velocity profile of the supersonic boundary layer flow, $M = 2.0$

Figure 12: Temperature profile of the supersonic boundary layer flow, $M = 2.0$

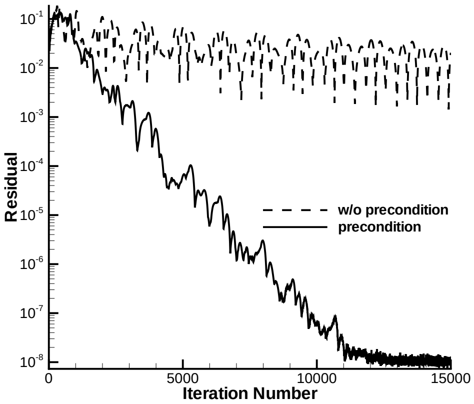

Figure 13: Convergence rate of the subsonic boundary layer flow, $M = 10^{-2}$

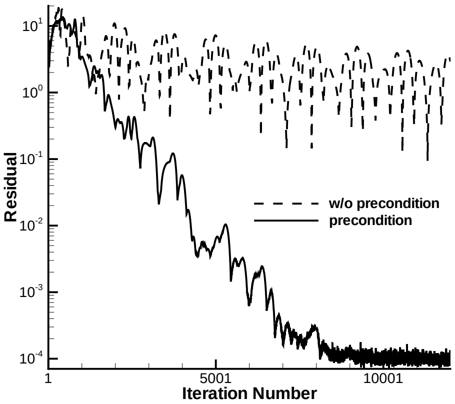

Figure 14: Convergence rate of the subsonic boundary layer flow, $M = 10^{-3}$

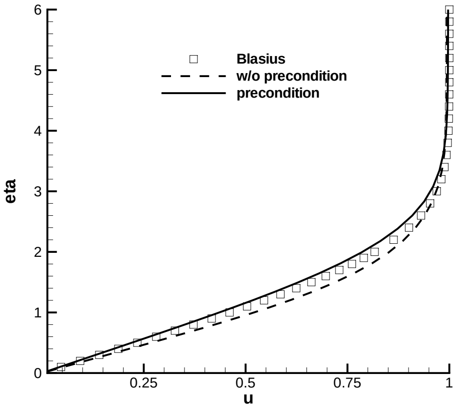

Figure 15: Velocity profile of the subsonic boundary layer flow, $M = 10^{-2}$

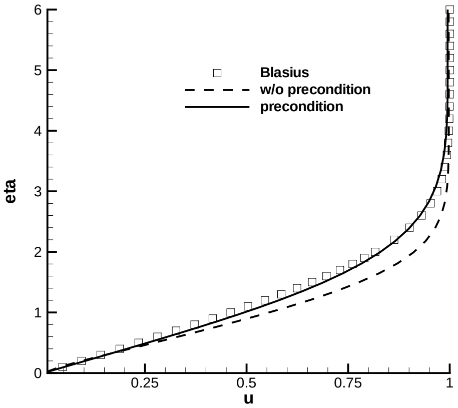

Figure 16: Velocity profile of the subsonic boundary layer flow, $M = 10^{-3}$

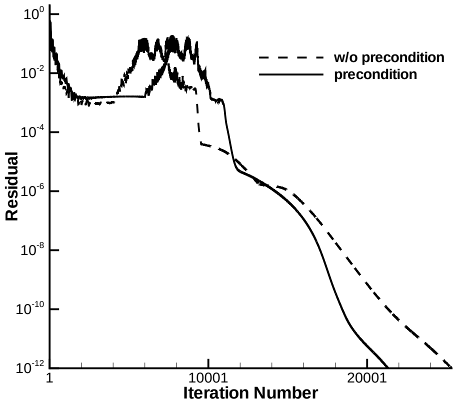

Figure 17: Convergence rate of the transonic converging-diverging nozzle flow

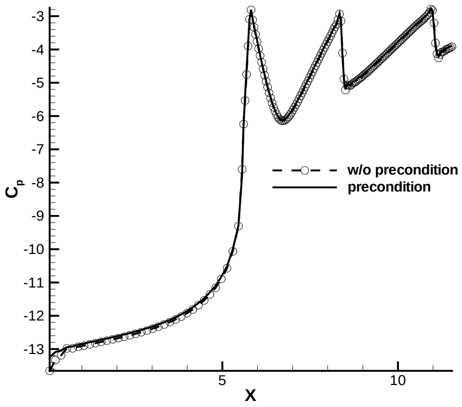

Figure 18: The pressure coefficients at the upper wall of the transonic converging-diverging nozzle flow

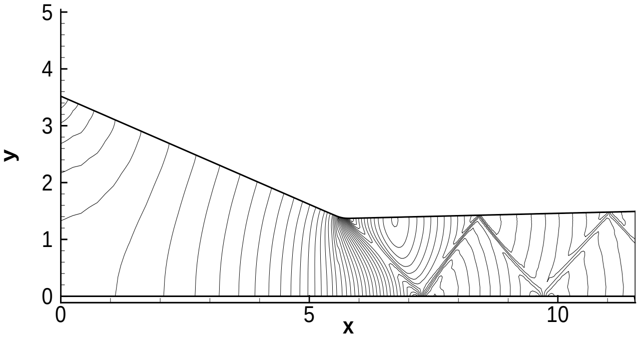

Figure 19: Mach number contours of the transonic converging-diverging nozzle flow

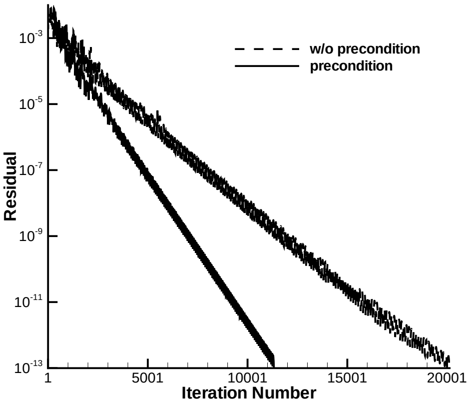

Figure 20: Convergence rate of the transonic flow over RAE2822 airfoil

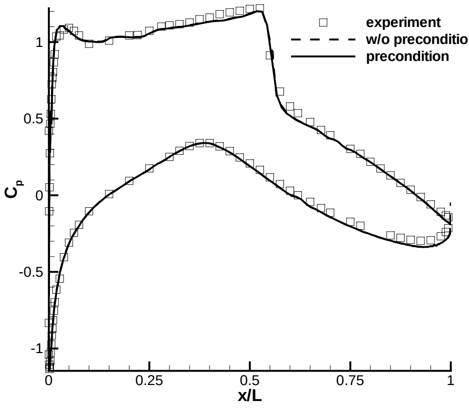

Figure 21: The pressure coefficients at the airfoil surface of the transonic flow over RAE2822 airfoil

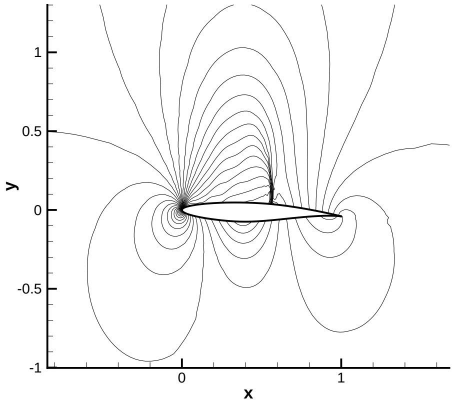

Figure 22: Pressure contours of the transonic flow over RAE2822 airfoil